Atmos. Meas. Tech. Discuss., https://doi.org/10.5194/amt-2017-234
Manuscript under review for journal Atmos. Meas. Tech.
Discussion started: 30 August 2017

Atmospheric Measurement Techniques Discussions
Open Access

Hotplate Precipitation Gauge Calibrations and Field Measurements

Nicholas Zelasko [1], Adam Wettlaufer [1], Bujidmaa Borkhuu [1], Matthew Burkhart [1], Leah S. Campbell [2], W. James Steenburgh [2], and Jefferson R. Snider [1, 3]

[1] University of Wyoming Department of Atmospheric Science

[2] University of Utah Department of Atmospheric Sciences

[3] Corresponding Author

Abstract –

First introduced in 2003, approximately 70 Yankee Environmental Systems (YES) hotplate precipitation gauges have been purchased by researchers and operational meteorologists. A version of the YES hotplate is described in Rasmussen et al. (2011; R11). Presented here is indoor- and field-based testing of a newer version of the hotplate; this device is equipped with longwave and shortwave radiation sensors. Hotplate surface temperature, coefficients describing natural and forced convective sensible energy transfer, and radiative properties (longwave emissivity and shortwave reflectance) are reported for two of the new-version YES hotplates. These parameters are applied in a new algorithm and used to derive liquid-equivalent accumulations for snowfall and rainfall; these accumulations are compared to values derived by the internal algorithm used in the YES hotplates (hotplate-derived accumulations) and to weighing gauge accumulations. In contrast with R11, the new algorithm accounts for radiative terms in a hotplate's energy budget, applies an energy conversion factor which does not differ from a theoretical energy conversion factor, and applies a surface area that is correct for the YES hotplate. Radiative effects are shown to be relatively unimportant for the precipitation events analyzed. In addition, this work documents a 10 % difference between the hotplate-derived and new-algorithm-derived accumulations. This difference seems consistent with R11's application of a hotplate surface area that deviates from the actual surface area of the YES hotplate and with R11's recommendation for an energy conversion factor that differs from that calculated using thermodynamic theory.

1 - Introduction

Two types of instrumentation have been developed for measuring liquid-equivalent snowfall rates and liquid-equivalent snow accumulations: 1) Weighing gauges that measure snowfall as it collects in a container or on a surface (WMO, 2008), and 2) optical gauges that measure the concentration and size of snow particles either in free fall or within a wind tunnel (Loffler-Mang and Joss, 2000; Deshler, 1988). Many of these gauges obstruct the wind and thus cause falling snow particles to deflect from the measurement zone. Consequently, rates and accumulations are underestimated and should be adjusted to account for undercatch (Jevons, 1861; Lovblad et al., 1993). Alternatively, both gauge types can be operated within a fenced enclosure that minimizes wind and the resultant undercatch (Goodison et al., 1998; Rasmussen et al., 2012). In addition, optical gauges require a snow particle density to convert concentration and size to a liquid-equivalent rate and accumulation (Brandes et al., 2007; Lempio et al., 2007). Because this density is variable and difficult to measure accurately (Locatelli and Hobbs, 1974), optical snowfall measurements are uncertain and remain uncertain even if undercatch is accounted for. A further disadvantage, for both the weighing and optical devices, is that the entrance to the device can become clogged with snow (Warnick, 1954; Currie, 1998; Stickel et al., 2005).

The Yankee Environmental Systems (YES, 2011) hotplate was developed to minimize the aforementioned uncertainties. Advantages of the hotplate are: 1) it is compact, 2) it is immune to clogging, 3) there is no requirement that snow particles fall through an opening, and 4) the derived rates and accumulations are largely independent of snow particle density, although a dependence does exist (R11; their figure 14).

This work furthers efforts to advance the hotplate as a snowfall measurement system (Borkhuu, 2009; R11; Boudala et al., 2014). We develop calibration constants for two hotplate systems configured with longwave and shortwave radiation sensors. These are a hotplate gauge owned by the University of Wyoming (UW) and a hotplate gauge owned by the National Center for Atmospheric Research (NCAR; Boulder, CO). In addition, we develop a new hotplate data processing algorithm, derive liquid-equivalent rates and accumulations for 27 precipitation events (snowfall and rainfall), compare accumulations obtained with the new algorithm to those derived by an internal algorithm (hotplate-derived accumulations), and compare accumulations to values derived using weighing gauges.

2 - Algorithm Development

The two vertically-stacked circular aluminum plates seen in Fig. 1 are the precipitation measurement portion of the YES hotplate system. The plate diameter (D_h) is 0.130 m and both plates have concentric rings that extend vertically either 3 mm (inner and middle rings) or 1 mm (outer ring) from the plate surface. One of the plates faces upward and is exposed to precipitation, the other faces downward. Temperature sensors monitor the top and bottom plates and feedback-controlled heaters maintain the plates at approximately 75 °C (R11). Electrical power supplied to the top plate (Q_{top}) compensates for power lost via sensible, net radiative, and latent (vapor mass) transfer. The power input to the bottom plate (Q_{bot}) is the source term in that plate's energy budget and is assumed to only compensate for sensible power output. This compensation is the basis for the hotplate's determination of wind speed (U). Values of U are commonly used to evaluate a Reynolds number (Re). The Reynolds number controls sensible heat transfer from a ventilated surface (Kobus and Wedekind, 1995). A complete description of our nomenclature is provided in the Appendix.

Since the hotplate was introduced in 2003, two teams (Borkhuu, 2009; R11) have reported data processing algorithms. The algorithm in Borkhuu (2009) can be explained by reference to the equation she used to model the top plate's power budget:

$0 =$	Implied Steady-state	
Q_{top}	Electrical Power Supplied to Top Plate	
$- D_h \cdot K_x \cdot (T_h - T) \cdot (\gamma + \alpha \cdot Re^{\beta})$	Sensible Power Output	
$- P \cdot E / f_2$	Latent Power Output	(1)

In Eq. 1, there are three terms that sum to zero in an assumed steady-state. The last of these, the latent power output, is proportional to the precipitation rate (P) and a snow particle catch efficiency (E) and inversely proportional to f_2, an electrical-to-precipitation conversion factor. In addition, the sensible power output term has contributions from natural convection (proportional to γ) and forced convection (proportional to $\alpha \cdot Re^{\beta}$), where α, β, and γ are fitted constants. These convective regimes are discussed in Kobus and Wedekind (1995) and are shown graphically in their Figure 6. Eq. 1 is similar to the algorithm used by King et al. (1978) to derive cloud liquid water concentration using a heated airborne sensor.

The algorithm in R11 is based on Eq. 2.

$$P = [Q_{top} - Q_{bot} - f_1(U)] \cdot f_2 / E \tag{2}$$

Here, $f_1(U)$ is a wind speed-dependent function. Also in Eq. 2, we see the conversion factor introduced in the previous paragraph. Somewhat different from how R11 formulated their conversion factors for rain and snow, we formulate f_2 to account for the warming of ice, melting, warming of the liquid, and liquid evaporation. For rain, we formulate f_2 to account for the warming of liquid and its evaporation. With an exception that we justify later, we applied the conversion factors as recommended by R11: 1) if $T < 0$ °C, the snow f_2 is applied, and 2) if $T > 4$ °C the rain f_2 is applied.

In Eq. 1, the sensible term is a function of *Re*, and thus *U*, and also a function of *T*. Hence, Eq. 1 can be rearranged to look similar to Eq. 2 with *P* dependent on *T*, *U*, Q_{top}, f_2, and *E*. A difference between the Eq. 1 and Eq. 2 formulations is the explicit dependence on Q_{bot}, in Eq. 2; this is in addition to the implicit Q_{bot}-dependent wind speed in *Re* (Eq. 1) and in $f_1(U)$ (Eq. 2).

Borkhuu (2009), YES (2011), and R11 surmised that the energetic effect of longwave and shortwave radiation could, in some settings, be comparable to the latent power term. Consequently, our hotplate (Wolfe and Snider, 2012) was upgraded by YES in 2011. The upgrade included radiation sensors for the measurement of longwave and shortwave fluxes. An objective of this paper is the incorporation of the radiation measurements into a new precipitation rate algorithm.

The following budget equation is the basis for our analysis:

$0 =$	Implied Steady-state
Q_{top}	Electrical Power Supplied to Top Plate
$- D_h \cdot K_x \cdot (T_h - T) \cdot (\gamma + \alpha \cdot Re^{\beta})$	Sensible Power Output
$- A_h \cdot \varepsilon_h \cdot \sigma \cdot T_h^4$	Longwave Power Output
$+ A_h \cdot \varepsilon_h \cdot IR_d$	Longwave Power Input
$+ A_h \cdot (1 - R_h) \cdot SW$	Shortwave Power Input
$- P \cdot E / f_2$	Latent Power Output (3)

Compared to Eq. 1, Eq. 3 has three additional terms. These describe the interaction of the hotplate with its environment via radiative transfer. Two of these terms are inputs (longwave and shortwave) and one is an output (longwave).

2.1 - Hotplate Data Files

The hotplate outputs data to two files. The previously discussed Q_{top} and Q_{bot} are two of several recorded variables and both of these are essential for the analysis described here. One of the files is known as the UHP or "user" hotplate file. The UHP file is provided to all YES customers. The second file is the SHP or "sensor" file. Table 1 has the list of all recorded variables and how some of these are symbolized. A complete list of variables (measured and computed), and constants, is provided in the Appendix. With the exception of Unix time, all variables in Table 1 are available as 60-s running averages, sampled at 1 Hz (YES, 2011).

2.2 - Radiative Properties

Two radiative properties are applied in this analysis. In the infrared, or longwave, the emissivity of the hotplate is the relevant property. The material used to fabricate the plates is aluminum, which when exposed to air becomes covered with an aluminum oxide layer. Hence, the hotplate emissivity was taken to be that of oxidized aluminum. The value we picked is ε_h = 0.14 (Weast, 1975; Section E). Furthermore, we made two assumptions: 1) the longwave output (Eq. 3) is the product of ε_h (assumed constant), hotplate area (A_h), and the flux emitted by a black body at T_h, and 2) the longwave input (Eq. 3) is the product ε_h, A_h and the downwelling longwave flux (IR_d). In a later section, we explain how we derive IR_d.

In the visible, or shortwave, the hotplate's reflectance (R_h) is the relevant property. Eq. 3 shows how we factored into a hotplate's energy budget the reflectance, a measured shortwave flux (SW; Table 1), and A_h. A value for R_h was determined as follows. We exposed the UW hotplate to solar illumination, while measuring the solar flux, and then shaded the hotplate to establish a baseline for the determination of R_h. During these experiments, there was negligible wind and therefore natural convection dominated forced convection in the budget. The energy budget equation we used to analyze these measurements has three terms: Q_{top}, sensible power output, and solar input. In two experiments, the values R_h = 0.66 and R_h = 0.61 were derived. We apply the average of these (R_h = 0.63) in our analysis of measurements from both UW and NCAR hotplates. Because of the oxide layer, the derived reflectance is smaller than the value reported for polished aluminum reflecting "incandescent" light (0.69; Weast, 1975; Section E) and significantly smaller than the value for vacuum-deposited aluminum at visible wavelengths (0.97; Hass, 1955).

3 - Methods

3.1 - Site Description

Indoor testing was conducted in a high-bay weather balloon hangar and in a laboratory. These facilities are at the University of Wyoming (UW) and are abbreviated hangar and lab. During wintertime, and especially at night, the hangar is cold (~ 0 °C); the lab is warm year round (~ 20 °C). Field measurements (Table 2) were conducted in Southeast Wyoming at the Glacier Lakes Ecosystem Experiments Site (GLE), in Southeast Wyoming near the summit of Battle Pass (BTL), and at the North Redfield site in Western New York (OWL). During both indoor and field measurements, all parameters reported by the hotplate (UHP and SHP variables; section 2.1) were recorded using a custom-built data system.

The accuracy of a hotplate-estimated precipitation rate is dependent on assessment of whether the sensed hydrometeors are rain or snow (R11 and Fig. 3a). We infer the latter using a calculated ice-bulb temperature (T_{IB}) (Iribarne and Godson, 1981; Chapter 7). Our basis for the T_{IB}s are measurements of relative humidity (RH; 100 % when saturated with respect to liquid), temperature, and pressure (Table 1). The lower limits on the T_{IB}s, assuming the measured RH is overestimated by 5 % (YES, 2011), is no more than 0.4 °C colder than the values we report. In instances with lower-limit T_{IB}s larger than 0 °C, we assume the sensed hydrometeors were liquid.

3.2 - NOAH-II Gauge

The NOAH-II is a weighing-type gauge manufactured by ETI Instrument Systems Inc. (www.etisensors.com). NCAR operated a NOAH-II at GLE and BTL during 2012, and coauthors (Campbell and Steenburgh) operated a NOAH-II at OWL (Dec. 2013 through Jan. 2014; Campbell et al., 2016). The three NOAH-II gauges were outfitted with Alter shields (Goodison et al, 1998; hereafter G98).

3.3 – Indoor Testing

Indoor testing of the UW hotplate was conducted every year from 2011 to 2015; the NCAR hotplate was only tested in 2012. Based on our testing of the UW hotplate, we have no evidence indicating that the calibration changed over the duration of any of the field deployments; however, Wettlaufer (2013) does demonstrate that calibration constants did change over the 2011 to 2015 interval in response to servicing conducted twice at YES. In this paper we present and apply calibration constants appropriate for the UW hotplate sensor deployed at GLE (April 2012) and at OWL (December 2013 through January 2014).

During testing, we controlled the hotplate's radiation environment by placing a material with known emissivity (painted-steel sheeting, $\varepsilon_s = 0.84$) above and below the hotplate. The steel sheets were positioned to dominate the hotplate's upward and downward fields of view (Fig. 2); however, the sheets were positioned vertically so that they were not heated by the hotplate. In that case, the sheet temperature (T_s) can be assumed equal to T.

Atmos. Meas. Tech. Discuss., https://doi.org/10.5194/amt-2017-234
Manuscript under review for journal Atmos. Meas. Tech.
Discussion started: 30 August 2017

3.4 - Downwelling Longwave Flux

As we have already mentioned, previous work concluded that the hotplate method of determining precipitation amount can be affected by longwave radiation. In response to that finding, YES incorporated a device that measures the net downward longwave flux (pyrgeometer, e.g., Albrecht et al., 1974) into the system (Table 1).

$$M_{IR} = IR_d - IR_u \quad (4)$$

The left-hand side of Eq. 4 represents the longwave radiant measurement (M_{IR}) and the right-hand side has the downward and upward components contributing to M_{IR}.

Because IR_d appears in the hotplate's budget (Eq. 3), and since M_{IR} is the only term in Eq. 4 that is measured, the upwelling component (IR_u) must be evaluated. This is possible because the signal from the pyrgeometer is adjusted, within the hotplate electronics package, to make the source of the upwelling infrared flux a virtual blackbody at the ambient temperature (YES 2012, personal communication). In that case, IR_d can be formulated as

$$IR_d \;=\; M_{IR} + \sigma \cdot T^4 \quad (5)$$

where σ is the Stefan-Boltzmann constant and T is the hotplate-measured ambient temperature. We also use Eq. 6 to calculate the downwelling infrared flux

$$IR_d \;=\; \varepsilon_s \cdot \sigma \cdot T_s^4 \quad (6)$$

3.5 – Warm-Cold Ambient Temperature Tests

Procedures described here were applied during testing conducted indoors (hangar and lab, section 3.1) at two different temperatures and are hereafter referred to as the warm/cold test. We show how values of a warm (T_w) and cold (T_c) ambient temperature, combined with other recorded hotplate variables (Table 1), can be used to derive two settings in Eq. 3 (T_h and γ). In our analysis, the temperature of the steel sheeting (T_s) is assumed equal to the ambient temperature (either T_w or T_c) and IR_d is calculated with Eq. 6. By design these tests had negligible forced-convective and latent transfers. In that case, Eq. 7a - b are the budget equations.

$$0 = Q_{top,w} - D_h \cdot K_x \cdot (T_h - T_w) \cdot \gamma - A_h \cdot \varepsilon_h \cdot \sigma \cdot T_h^4 + A_h \cdot \varepsilon_h \cdot \varepsilon_s \cdot \sigma \cdot T_w^4 + A_h \cdot (1 - R_h) \cdot SW_w \quad (7a)$$

$$0 = Q_{top,c} - D_h \cdot K_x \cdot (T_h - T_c) \cdot \gamma - A_h \cdot \varepsilon_h \cdot \sigma \cdot T_h^4 + A_h \cdot \varepsilon_h \cdot \varepsilon_s \cdot \sigma \cdot T_c^4 + A_h \cdot (1 - R_h) \cdot SW_c \quad (7b)$$

The measurements applied in these equations were T_w and T_c, the warm and cold plate powers ($Q_{top,w}$ and $Q_{top,c}$), the warm and cold shortwave fluxes (SW_w and SW_c), and constants (Appendix). Values of T_h and γ (hereafter referred to as T_h/γ pairs) were derived by minimizing departures from zero simultaneously in Eq. 7a - b. Minimization was conducted using a Newton's method equation solver (Exelis Visual Information Solutions, Inc.); the convergence tolerance was 1×10^{-4} J s^{-1}.

3.6 - Nusselt-Reynolds Relationship

The Nusselt number ($Nu = \gamma + \alpha \cdot Re^{\beta}$), is a component of the sensible power output term in Eq. 3. In this section, we develop a relationship between Nu and Re based on measurements recorded in the field when precipitation was not occurring; in a later section we show how that relationship is applied in a calculation of the precipitation rate.

Conceptually, Nu is a dimensionless representation of the sensible power output. Eq. 8a was used to calculate Nu with measurements (Q_{top}, T, and SW), a calculated variable (IR_d; section 3.4), and constants (Appendix and Table 3).

$$Nu = [Q_{top} - A_h \cdot \varepsilon_h \cdot \sigma \cdot T_h^4 + A_h \cdot \varepsilon_h \cdot IR_d + A_h \cdot (1 - R_h) \cdot SW] \,/\, [D_h \cdot K_x \cdot (T_h - T)] \quad (8a)$$

In the denominator of Eq. 8a is a term proportional to the sensible power output due to molecular conduction.

Conceptually, *Re* is a dimensionless representation of the wind speed. Eq. 8b was used to calculate *Re* with a measurement (*U*) and constants (Appendix).

$$Re = p_x \cdot D_h \cdot U \,/\, (R_d \cdot T_x \cdot \mu_x) \qquad (8b)$$

Two criteria were used to select a site-specific data subset for the *Nu*-*Re* development: 1) no precipitation, and 2) at least three hours of continuous measurements with a broad range of wind speeds. We fitted the selected *Nu*-*Re* pairs using a non-linear least squares procedure (curvefit; Exelis Visual Information Solutions, Inc.); the convergence tolerance for the relative decrease in chi-squared was 1×10^{-3}.

3.7 - Electrical-to-precipitation Conversion Factor

Equilibrium thermodynamics, with the assumptions that ice melts at T_o = 0 °C and vaporization occurs at T_h, was used to derive the conversion factor in Eq. 3 (f_2). Adopting the temperature criteria from R11 (also see section 2), and a framework from Iribarne and Godson (1981; Chapter 7), we formulated theoretical conversion factors as

$$f_2(T, T_h) = \{\rho \cdot A_h \cdot [\, C_i \cdot (T_o - T) + L_f(T_o) + C \cdot (T_h - T_o) + L_v(T_h)]\}^{-1} \quad (T < 0\ ^{\circ}\mathrm{C}) \qquad (9a)$$

$$f_2(T, T_h) = \{\rho \cdot A_h \cdot [\, C \cdot (T_h - T) + L_v(T_h)]\}^{-1} \quad (T > 4\ ^{\circ}\mathrm{C}) \qquad (9b)$$

This formulation is graphed in Fig. 3a (solid line) where we extended Eq. 9b into the temperature range (0 °C < T < 4 °C) where the distinction between rain and snow is ambiguous because falling snow particles remain unmelted in situations with T > 0 °C and low humidity (R11).

We now compare the conversion factor derived using Eq. 9a – b with that reported in R11. To be consistent with R11, we assume $T = T_h$ = 0 °C. We find that the ratio of f_2 (Eq. 9a) divided by the factor reported in R11 for snow (3.99×10^{-8} m J^{-1}) and the ratio of f_2 (Eq. 9b) divided by the factor reported in R11 for rain (4.52×10^{-8} m J^{-1}), are both 0.666. Since these

Atmos. Meas. Tech. Discuss., https://doi.org/10.5194/amt-2017-234
Manuscript under review for journal Atmos. Meas. Tech.
Discussion started: 30 August 2017

Atmospheric Measurement Techniques Discussions

ratios are equal to the area in R11 (A_h = 0.008844 m^2), divided by the area applied in our calculation ($A_h = (\pi/4)\cdot 0.130^2$ = 0.01327 m^2), we conclude that the discrepancy is not due to differing thermodynamic parameters applied in R11's and our calculations (e.g., the latent heat of vaporization), rather it stems from the different values used for the hotplate area. Further, R11 changed their theoretical f_2 to an actual conversion factor that was "..lower because of the imperfect heat transfer from the precipitation to the hot plate (losses to the air, e.g.)." We do not find justification for this in R11, nor do we agree with R11's assignment of A_h = 0.008844 m^2 assuming they were recommending that value for the hotplate sold by YES. Recently, Boudala et al. (2014) addressed the second of these two points, making it clear that A_h = 0.01327 m^2 is appropriate for the hotplate sold by YES.

In light of the above, the ratio of our f_2 (Eq. 9a – b with $T = T_h$ = 0 °C), divided by the actual conversion factor in R11, is 0.86 for snow and 0.89 for rain. Since a derived precipitation rate is proportional to f_2 (e.g., Eq. 2), we expect the ratio of a precipitation rate from the new algorithm (assuming $T = T_h$ = 0 °C), divided by a synchronous hotplate-derived precipitation rate, to be between 0.86 and 0.89. Our expectation hinges on the assumption that the YES algorithm has incorporated R11's surface area and R11's distinction between theoretical and actual conversion factors.

We calculate f_2 in the new algorithm two ways: 1) In a comparison made to a hotplate-derived accumulation, our f_2 is set to 2.66 × 10^{-8} m J^{-1} (snow) and 3.01 × 10^{-8} m J^{-1} (rain). These values were obtained from Eq. 9a – b with $T = T_h$ = 0 °C and are displayed as a dotted line in Fig. 3a. 2) In comparisons made to either a NOAH-II accumulation or to a laboratory reference precipitation rate, we evaluate f_2 using Eq. 9a – b with a T_h from Table 3 and with the hotplate-measured ambient T (Table 1). In addition to the step change due to the difference between the

Atmos. Meas. Tech. Discuss., https://doi.org/10.5194/amt-2017-234
Manuscript under review for journal Atmos. Meas. Tech.
Discussion started: 30 August 2017

Atmospheric Measurement Techniques Discussions

latent heats of sublimation and vaporization, our conversion factor has a weak temperature dependence (Fig. 3a, solid line). This is accounting for the warming discussed in section 2. Also, in Fig. 3a we display the actual conversion factor from R11 (dashed line). Our classification of measurements into snow and rain is discussed in a later section.

3.8 – Snow Particle Catch Efficiency

The hotplate's snow particle catch efficiency (*E*; section 2) is accounted for using a wind speed-dependent function (R11). The function accounts for the fact that snow particles landing on the hotplate can bounce, and be carried away by the wind, or be sheared off by the wind after they land. This conceptual description of catch on the hotplate is different from that used to describe catch by weighing gauges where undercatch results because a subset of snow particles are carried over the gauge by a vertically-accelerated flow (Nespor and Servuk, 1999; Thériault et al., 2012). Both R11 and G98 derive catch efficiencies as the ratio of two paired values of liquid-equivalent accumulation, one obtained from the gauge of interest and the other obtained from a second gauge operated inside a Double Fence Intercomparison Reference Shield (DFIR).

The snow particle catch efficiency functions applied here are both gauge- and location-dependent. For the UW hotplate (at GLE and OWL), and the NCAR hotplate (at BTL), we apply the function recommended by YES (YES 2012, personal communication; hereafter Y12). Wind speeds used in the efficiency calculation are the hotplate-derived *U*. In addition, the hotplate catch efficiency function described by R11 (their Equation 6) was also applied. This is based on the hotplate *U* adjusted to the 10-m level with a roughness length z_o = 0.3 m (G98, their Equation 4.3.1) and was only used in analysis of measurements made at OWL. The z_o we picked corresponds to a surface with "Many trees, hedges, few buildings" (Panofsky and Dutton, 1984; their Figure 6.2). This assignment is consistent with the presence of shrubs and trees (Steenburgh et al., 2014), and a two-story barn, at the OWL site. The barn was located at the eastern edge of a fallow field, 80 m west of the gauges at OWL. For the NOAH-II gauge, we applied a function developed for an 8-inch (diameter) Alter-shielded gauge (G98; their Equation 4.7.1). Wind speeds used in that calculation are from the hotplate (at GLE and BTL) or from an anemometer (at OWL) (Campbell et al., 2016). Of course, we are assuming that the function from G98 mimics undercatch by our 12-inch (diameter) Alter-shielded NOAH-II gauge.

In Fig. 3b, we present the three catch efficiency functions (R11 with U adjusted to 10 m, Y12, and G98). In this graph, the wind speed applied in the R11 function is the value plotted on the abscissa multiplied by 2.9. This adjustment corresponds to the lowest installation of the hotplate at OWL and decreases to 2.0 for measurements made after 20131217 [1]. In our calculation of the R11 catch efficiency functions, the snow depth for the interval of interest (20131211 to 20140129) was set equal to the average (0.7 m) derived using an ultrasonic snow depth instrument operated at OWL (Campbell et al., 2016). This average, and the AGL altitudes of the hotplate installation (Table 2), were used to derive the two wind-speed adjustment factors (2.9 and 2.0). The basis for this calculation is G98's gauge-height correction formula (their Equation 4.3.1).

Since the anemometer at OWL was operated at nearly the same height as the top of the NOAH-II gauge (Steenburgh et al., 2014), and the G98 catch efficiency formula (their Equation 4.7.1) assumes speeds are measured at the height of the gauge opening, a vertical adjustment of the wind speed was not factored into the G98 catch efficiencies.

[1] Altitudes of the two hotplate installations are provided in Table 2.

4 – Testing and Calibration Results

4.1 – Warm-Cold Tests

Results from the warm-cold tests are described here. The derived T_h/γ pairs (section 3.5) are in Table 3. The T_h values are 42.2 °C for the NCAR hotplate deployed at BTL (NCAR/BTL), 52.2 °C the UW hotplate deployed at (UW/GLE), and 65.5 °C for the UW gauge deployed at OWL (UW/OWL). The first two T_hs differ from those presented in Wettlaufer (2013) where, for the NCAR hotplate, he reported agreement with the nominal plate temperature (75 °C; R11) and for the UW hotplate (GLE) he reported a larger temperature (T_h = 109 °C). The T_h/γ pair reported in Table 3, for the UW/OWL study, was evaluated after Wettlaufer (2013) reported his warm-cold test results.

In our analysis of the warm-cold measurements we only used data acquired in the hangar; Wettlaufer (2013) analyzed both hangar and lab data. For us the warm-cold temperature pairings are 5.4/-4.3 °C (NCAR/BTL), 7.0/-1.1 °C (UW/GLE), and 29.5/10.4 °C (UW/OWL). Compared to Wettlaufer (2013), our T_ws are 15 °C colder (NCAR/BTL and UW/OWL experiments only). Using our T_h/γ pairs (Table 3) and the first two T_ws (i.e., for NCAR/BTL and UW/GLE), we evaluated the term in Eq. 7a representing natural-convective transfer ($D_h \cdot K_x \cdot (T_h - T_w) \cdot \gamma$) and compared to values derived using T_h/γ pairs in Wettlaufer (2013; his Table 2). In the NCAR/BTL comparison T_w was set at 5.4 °C and in the UW/GLE comparison T_w was set at 7.0 °C. Our natural-convective term agrees within ± 0.1 W of those derived by Wettlaufer (2013). Also in good agreement is the product of T_h and γ. Relative to Wettlaufer (2013), our $T_h \times \gamma$ product is 6 % larger (NCAR/BTL), and 7 % larger (UW/GLE). We expect that our T_h/γ pairs (Table 3), when applied in Eq. 3, will produce a reasonable estimate of the precipitation rate. We test that expectation in the next section.

Error limits on T_h and γ, in Table 3, were derived by perturbing $Q_{top,w}$ (i.e., the value acquired in the warm test) by ± 0.5 W and repeating the analysis (Eq. 7a - b). Our estimate of the $Q_{top,w}$ error (± 0.5 W) came from a comparison of values acquired before and after power to the hotplate was stopped and restarted. These tests were conducted in the hangar and the 10 min warm up recommended by the manufacturer was adhered to (YES, 2011).

4.2 - Drip Tests

This section compares two time sequences of precipitation rate: one calculated with the new algorithm, the other is the hotplate-derived value (Table 1). The basis for the comparison is measurements of artificially-produced liquid precipitation made in the hangar. We applied water drops to the NCAR and UW hotplates using a volumetric water pump (Ismatec Inc.; Model 7618). Each of these tests has a drip period (4 min) and a nondrip period (5 min). Drops (4 mm volume-equivalent diameter) were added uniformly to the top plate at a constant volumetric rate. Assuming all of the pumped water is delivered to the hotplate, the pump rate is proportional to a precipitation rate. We see no reason to question this assumption. Hence, we convert the pump rate to a reference precipitation rate (P_{REF}) and apply the P_{REF} in subsequent analyses [2]. These drip tests were conducted at T > 4 °C.

Because the drip tests were conducted with the hotplate operating as in Fig. 2, and unventilated, the recorded data were analyzed with $T_s = T$, in Eq. 6 (section 3.5), and with the sensible power output formulated as $D_h \cdot K_x \cdot (T_h - T) \cdot \gamma$ (Appendix and Table 3). Also, because all

[2] The value of the multiplier that converts the volumetric pump rate (cm^3 min^{-1}) to precipitation rate (mm hr^{-1}) is 4.51.

Atmos. Meas. Tech. Discuss., https://doi.org/10.5194/amt-2017-234
Manuscript under review for journal Atmos. Meas. Tech.
Discussion started: 30 August 2017

of the pumped water is delivered to the top plate, the catch efficiency is $E = 1$. With these constraints, precipitation rates were derived by inputting measurements (Q_{top}, T, U, and SW) and a calculated variable (IR_d; section 3.4) into Eq. 3 and solving for a precipitation rate sequence ($P(t)$). We symbolize this $P(t)$ as P_{UW} and refer to calculations leading to that sequence as the UW algorithm. Also, we refer to sequences obtained from the UHP file (Table 1) as P_{YES} and refer to that calculation as the YES algorithm.

We now compare values of P_{UW} to synchronous values of P_{YES}. Typically, these rates exhibit a maximum ~ 3 min after the nondrip-to-drip transition (Fig. 4). We interpret these maxima as overestimates, possibly due to a violation of the steady-state assumption. Also evident, particularly in the P_{UW} sequence, is a minimum. This occurs during the time the instrument is relaxing to its rest state; i.e. ~ 2 min after a drip-to-nondrip transition. The figure also demonstrates that thresholding is applied to the P_{YES} sequence, i.e. the YES algorithm thresholds the output to 0 mm hr^{-1} if values decrease to < 0 mm hr^{-1}. This is evident at ~ 16:11 UTC and at three other times in the P_{YES} sequence.

Two 1-min averaging intervals are shown in Fig. 4. We set the end of these at the drip-to-nondrip transitions. Fig. 5 is a compilation of the two tests already discussed (Fig. 4) plus four additional P_{REF} vs $\langle P_{UW} \rangle$ comparisons and four additional P_{REF} vs $\langle P_{YES} \rangle$ comparisons.

We now use linear least-squares regression analysis, and a regression equation of form $y = a \cdot x$, to derive the ratio of two precipitation rates. In Fig. 5 it is apparent that the regression slope (ratio), derived for the P_{REF} vs $\langle P_{UW} \rangle$ comparison, does not differ from one by more than ± 1 standard deviation. Ratios for the two hotplates (UW and NCAR) and for three drip tests are summarized in Table 4. In the third column (P_{REF} vs $\langle P_{UW} \rangle$), we see that none of the ratios differ from one by more than ± 1 standard deviation. Different from Fig. 5 and Table 4, we also evaluated intercepts of regressions that were not forced through the origin; none of these intercepts differ significantly from zero (results not shown). From the statistical comparisons in Table 4, we conclude the T_h/γ pairs (Table 3) applied in the UW algorithm (Eq. 3) produce a precipitation rate consistent with the reference.

Values of the reference rate and the hotplate-derived rate ($<P_{YES}>$) are compared as ratios in Fig. 5 and in the fourth column of Table 4. These ratios are seen to deviate systematically from unity and in the direction discussed in section 3.7. In the unforced regressions (not shown) the intercepts are negative, but only one of these differed significantly from zero (NCAR/BTL; intercept = -0.3 ± 0.1). Negative intercepts are expected because P_{YES} is positively offset, by ~ 0.2 mm hr^{-1}, during most of the nondrip periods (e.g., 16:21 UTC in Fig. 4).

5 - Field Measurements

This section is organized as follows: Section 5.1 presents field measurements of ambient temperature and ambient ice-bulb temperature. We use this information to classify 27 precipitation events as snowfall or rainfall. Section 5.2 presents the *Nu-Re* relationship we use to account for the sensible power term in Eq. 3. Section 5.3 describes how we derive a precipitation rate for a hotplate based on measurements made in the field. Section 5.4 compares time-integrated precipitation rates (accumulations) derived using the two algorithms. In section 5.4, we also compare hotplate accumulations to values from the NOAH-II.

5.1 – Field-measured Temperatures and Ice-bulb Temperatures

The 27 precipitation events are summarized in Table 5. Measurements were made during 2012, at the two Southeast Wyoming field sites (BTL and GLE), and during 2013 and 2014 at the Western New York site (OWL). Table 5 and Fig. 6 have event-averaged ambient temperatures ($<T>$) and the event-averaged ambient ice-bulb temperatures ($<T_{IB}>$; section 3.1).

Atmos. Meas. Tech. Discuss., https://doi.org/10.5194/amt-2017-234
Manuscript under review for journal Atmos. Meas. Tech.
Discussion started: 30 August 2017

Atmospheric Measurement Techniques Discussions

Twenty-three of the events have $\langle T \rangle \leq -3.3$ °C and upper-limit temperature ($\langle T \rangle$ plus two standard deviations) no warmer than -2.3 °C. We classified these as snowfall. In addition, we classified four events as rainfall. These had $\langle T_{IB} \rangle \geq +2.9$ °C and lower-limit temperature ($\langle T \rangle$ minus two standard deviations) no colder than +2 °C.

5.2 - Nusselt-Reynolds Relationship

Fig. 7b shows a plot of the *Nu*-*Re* fit function with the data used to constrain the function. This result is for the UW hotplate operating at the GLE site. Fit coefficients (α, β, and γ) are reported in Table 6 for each field site. Hansen and Webb (1992) reported α = 0.09 and a β between 0.69 and 0.72 for a surface similar to the hotplate (circular with three concentric rings); however, their flow direction was perpendicular to the plate surface. The values of α and β we report may differ from those in Hansen and Webb (1992) because the flow is principally parallel to the plate surface at our field sites. There are two other differences relative to Hansen and Webb (1992): 1) Our geometrically-averaged *Nu* (~ 360) is about a factor of five larger, and 2) our *Re* extends smaller by a factor of two and larger by a factor of three. Finally, we note that compared to Fig. 7b there is an order of magnitude narrower *Re* range in the NCAR/BTL and UW/OWL *Nu*-*Re* plots (not shown).

Fig. 7a is a companion to Fig. 7b showing the γ based on the warm-cold test. The error limit on this datum is explained in section 4.1. Since *Nu* is dependent on the T_h derived in the warm-cold test (section 3.5), we expect the *Nu*-*Re* function to converge to the warm-cold γ in the limit of small *Re*. In our assessment of convergence, we evaluated the limiting *Nu* at the *Re* corresponding to the minimum *U* reported in the hotplate data output (0.1 m s^{-1}). This minimum *U* establishes the left end of the function in Fig. 7b. Convergence of the *Nu*-*Re* relationship to within the error limit on the warm-cold γ, at the former's left-most limit, is evident in Fig. 7a – b.

Atmos. Meas. Tech. Discuss., https://doi.org/10.5194/amt-2017-234
Manuscript under review for journal Atmos. Meas. Tech.
Discussion started: 30 August 2017

Convergence is also evident in the NCAR/BTL and UW/OWL plots analogous to Fig. 7a – b (not shown) and this in spite of narrower *Re* range in those datasets.

5.3 - Precipitation Rate from Field Measurements

Fig. 8 shows energy-budget terms (Eq. 3) for one of the four rainfall events in our dataset (OWL-15 in Fig. 6). The three output terms (sensible, latent, and upwelling longwave), and three input terms (top plate power, downwelling longwave, and shortwave) are shown in Fig. 8a - b. In this section we begin with the sequence of latent power output (i.e., the sequence labeled $P{\cdot}E/f_2$ in Fig. 8a) and describe how we calculate the sequence of rainfall rate. We also contrast that calculation with steps followed in the case of snowfall.

The first step in the calculation is conversion of the latent term (Fig. 8a) to a provisional precipitation rate; this is done by multiplying each element of the latent term by the corresponding element of f_2 (Eq. 9b). This operation is referred to as element-by-element vector multiplication. Thresholding is applied next. Both a 300-s running average of the provisional rate and a 10-s running average of the provisional rate are computed. If the 300-s average exceeds 0.25 mm hr^{-1}, and the 10-s average exceeds 0 mm hr^{-1}, the rate is stored as the 10-s average; otherwise the rate is stored as 0 mm hr^{-1}. We refer to the resultant as P_{UW}, but we note that in section 4.2 the P_{UW} sequences were unthresholded. Both the thresholded and unthresholded sequences are presented in Fig. 8c – d. The thresholded P_{UW} is identical to the unthresholded P_{UW} where the 300-s average exceeds 0.25 mm hr^{-1} and the 10-s average exceeds 0 mm hr^{-1}.

In the case of snowfall, the f_2 is calculated using Eq. 9a and applied as discussed in the previous paragraph. Finally, the precipitation rate is derived as the resultant of element-by-element vector multiplication of the thresholded P_{UW} and the reciprocal of the snow particle catch efficiency (section 3.8).

5.4 – Comparisons of Liquid-equivalent Accumulation

Here we use linear least-squares regression analysis, with a regression equation of form $y = a \cdot x$, to derive the ratio of two measures of liquid-equivalent accumulation for snow. In Fig. 9, these measures are the accumulations derived using the UW and YES algorithms. In the these algorithms the particle catch efficiency function is the one described in Y12 and f_2 is 2.66×10^{-8} m J^{-1}(section 3.7). The data points correspond to measurements made at GLE (UW hotplate), at BTL (NCAR hotplate), and at OWL (UW hotplate). We note that 19 of 23 *y*-axis values are from the same instrument (UW hotplate) and are derived using the same calibration (UW/OWL) applied to produce the result shown in the third row of Table 4. Statistical consistency between the ratio in Fig. 9 (0.79 ± 0.05) and the ratio in the third row of Table 4 (i.e., 0.79 ± 0.03 for the P_{REF} vs $<P_{YES}>$ ratio) suggests a systematic error in the YES-derived precipitation rates and accumulations. This assertion is reinforced by the three NCAR hotplate points straddling the best-fit line, in Fig. 9, and by the ratio reported in Table 4 for the NCAR hotplate (i.e., 0.81 ± 0.03 for the P_{REF} on $<P_{YES}>$ ratio). However, we cannot exclude the possibility that bias in our field-based calibration coefficients (α, β, and γ; Table 6) is the reason for a UW/YES ratio significantly smaller than unity in Fig. 9.

As was discussed in section 4.2, and demonstrated in Fig. 4, during the indoor nondrip periods the P_{YES} sequence is positively offset. A plausible reason for this, and for the ratios < 1 reported in the previous paragraph, is disregard for longwave forcing in the YES algorithm. Since we do not have access to the YES algorithm, we estimated the longwave radiative effect by setting the downwelling and upwelling longwave terms to zero in Eq. 3. After doing this, a larger UW/YES ratio was obtained in a plot analogous to Fig. 9 (0.83 ± 0.04). From this modest increase of the UW/YES ratio, we conclude that offset due to longwave forcing *cannot* explain

Atmos. Meas. Tech. Discuss., https://doi.org/10.5194/amt-2017-234
Manuscript under review for journal Atmos. Meas. Tech.
Discussion started: 30 August 2017

Atmospheric Measurement Techniques Discussions

UW/YES ratios significantly smaller than unity. An even smaller-magnitude perturbation of the UW/YES ratios was obtained when zeroing the shortwave term in Eq. 3 (results not shown).

Further evidence for systematic error in the YES values comes from Fig. 10. With the exception that these data are for rain observed at OWL (section 5.1) the comparison in Fig. 10 is similar to Fig. 9. Although the number of points is small, Fig. 10 establishes that our finding of a UW/YES ratio significantly smaller than unity is true for both rainfall and snowfall. In addition, Fig. 11 strengthens this conclusion by showing agreement between values of UW algorithm accumulation and the NOAH-II accumulation when both gauges are detecting rain.

An additional assessment of snowfall at OWL is presented in Fig. 12a – c. In these graphs NOAH-II measurements are plotted on the abscissa and different interpretations of the UW hotplate measurements are plotted on the ordinate. For both devices, we plot the ratio of a liquid-equivalent accumulation divided by an event-averaged particle catch efficiency, and we note that the numerator of this ratio is an accumulation that was not corrected for inefficient catch [3] and that values contributing to these ratios are in Table 5. Table 5 demonstrates two features of the OWL snow data set: 1) The event-averaged catch efficiency based on Y12 (*<E Y12>*) is consistently larger than the event-averaged efficiency based on R11 (*<E R11>*), and 2) the event-averaged efficiency *<E R11>* is comparable to *<E Y12 An>*, where the latter is the event-averaged efficiency derived with the anemometer *U* and the Y12 catch efficiency function. These features are consistent with the altitude adjustment in R11, which increases the wind speed (section 3.8), and thus decreases *<E R11>* relative to *<E Y12>*. They are also consistent with a low bias in the hotplate-derived *U*. The latter is supported by a comparison of the hotplate *U* vs

[3] This comparison was also made using accumulations corrected with a time-dependent catch efficiency (section 5.3), but we found that the fit-line slopes differed by less than ± 5 % from those in Fig. 12.

anemometer U where the fit-line slope is 0.55 ± 0.05 for the 19 snow events at OWL (results not shown).

Consistent with the ranking of event-averaged Es (Table 5), Fig. 12a shows that the hotplate values, derived with the hotplate U and the Y12 catch efficiency function, are statistically smaller than the NOAH-II-derived values. We also see that the 15% statistical underestimate in the hotplate (Fig. 12a) reverses to a slight overestimate when using the R11 catch efficiency function (Fig. 12b) and when using the anemometer U with the Y12 function (Fig. 12c). Unfortunately, these results do not allow us to specify relative contributions to the 15% statistical underestimate (Fig. 12a) coming from the fact that the Y12 function does not use a height-adjusted U or from the suspected hotplate underestimate of U. Further studies focused on development of a hotplate catch efficiency function dependent on the local wind speed, as opposed to the wind speed at 10 m (R11), and investigation of the hotplate's determination of wind speed, are needed to resolve this issue.

6 - Conclusions

Measurements made with two YES hotplates were used to derive precipitation rates and accumulations for 27 snowfall and rainfall events. The basis for this is an energy budget equation similar to that in King et al. (1978). We changed that energy budget (Eq. 1) by including terms that describe longwave and shortwave radiant energy transfer (Eq. 3). To the best of our knowledge, this is the first time that radiative terms have been incorporated into a hotplate data analysis algorithm and reported in the scientific literature.

In this paper, we have used computational methods different from those in R11, and we derived and applied different calibration coefficients. In spite of these changes we report precipitation rates and accumulations that strongly correlate with the output of two YES hotplates. However, a systematic difference is evident in comparisons of the UW and YES algorithms. We surmise that the difference comes from the following: 1) R11's assignment of A_h (0.00884 m^2 vs 0.01327 m^2 in the UW algorithm), 2) R11's distinction between a theoretical and an actual energy conversion factor, and 3) the incorporation of #1 and #2 into the YES algorithm. Clearly, R11's A_h is not justified for hotplates sold by YES (Boudala et al., 2014; YES 2017, personal communication). R11's distinction between conversion factors is more problematic. That distinction can be interpreted two ways: either 1) The distinction accounts for environmental thermal energy input that assists the conversion of precipitation mass to vapor, or 2) the distinction accounts for the loss of snow particles from the top surface of the hotplate due to removal by wind. Because early in the warming process a precipitation element attains a temperature larger than that of the air, we assert that the first of these phenomena is unlikely to contribute significantly to the energy budget. The second may be significant, but it is our opinion that removal of precipitation mass by wind is best accounted with a catch efficiency, not with a distinction between conversion factors. Lastly, accounting for either of these phenomena, independent of an adjustment of the catch efficiency, should be accomplished with an increase of an actual conversion factor relative to the theoretical value, not with the decrease proposed by R11.

Acknowledgements -

We gratefully acknowledge the support provided by the UW Department of Atmospheric Science Engineering Group.We also thank Ontario Winter Lake-effect Systems (OWLeS) project PIs Bart Geerts and Dave Kristovich for their leadership and Philip Bergmaier for maintaining the hotplate during OWLeS. This work was supported by the United States National Science Foundation (Award EPS 1208909), the Wyoming Water Development Commission (Award WWDC40395H), and by the U.S. Department of Interior (Award 1000628L).

Atmos. Meas. Tech. Discuss., https://doi.org/10.5194/amt-2017-234
Manuscript under review for journal Atmos. Meas. Tech.
Discussion started: 30 August 2017

Appendix – Nomenclature

A_h	Area of YES hotplate = 0.01327 m^2
C	Liquid H_2O specific heat capacity = 4218 J kg^{-1} K^{-1} (assumed independent of temperature; Iribarne and Godson, 1981; their Table IV-5)
C_i	Solid H_2O specific heat capacity = 2106 J kg^{-1} K^{-1} (assumed independent of temperature; Iribarne and Godson, 1981; their Table IV-5)
D_h	Diameter of YES hotplate = 0.130 m
E	Snow particle catch efficiency (section 3.8)
f_1	Wind speed-dependent property in Eq. 2 [W]
f_2	Electrical-to-precipitation conversion factor [m J^{-1}]
IR	Component of longwave flux [W m^{-2}]
$L_f(T_o)$	Latent heat of fusion evaluated at the thermodynamic reference temperature = 0.3337x10^6 J kg^{-1} (Iribarne and Godson, 1981; their Table IV-5)
$L_v(T_h)$	Latent heat of vaporization at T_h (Iribarne and Godson, 1981; their Equation 4.103) [J kg^{-1}]
M_{IR}	Measured net longwave flux (section 3.4) [W m^{-2}]
Nu	Nusselt number
P	Liquid-equivalent precipitation rate [mm hr^{-1} or m^3 m^{-2} s^{-1}]
P_{Ref}	Reference precipitation rate (section 4.2) [mm hr^{-1} or m^3 m^{-2} s^{-1}]
P_{UW}	Precipitation rate derived with UW algorithm (section 5.3) [mm hr^{-1} or m^3 m^{-2} s^{-1}]
P_{YES}	Precipitation rate derived with YES algorithm (section 4.2) [mm hr^{-1} or m^3 m^{-2} s^{-1}]
Q_{bot}	Bottom plate power [W]
Q_{top}	Top plate power [W]
R_d	Dry air specific gas constant = 287 J kg^{-1} K^{-1}
Re	Reynolds number
R_h	Hotplate Reflectance = 0.63 (section 2.2)
SW	Measured shortwave flux (section 2.2) [W m^{-2}]
T	Ambient temperature [^{o}C or K]
T_h	Hotplate surface temperature (section 3.5) [^{o}C or K]

Atmos. Meas. Tech. Discuss., https://doi.org/10.5194/amt-2017-234
Manuscript under review for journal Atmos. Meas. Tech.
Discussion started: 30 August 2017

Atmospheric Measurement Techniques Discussions
Open Access
EGU

T_o	Thermodynamic reference temperature = 0.0 ^oC
T_s	Temperature of painted-steel sheeting [^{o}C or K]
U	Wind speed [m s^{-1}]

Greek Symbols

α	Fitted *Nu*-*Re* Coefficient (section 3.6)
β	Fitted *Nu*-*Re* Coefficient (section 3.6)
ε_h	Hotplate emissivity = 0.14 (section 2.2)
ε_s	Emissivity of painted-steel sheeting = 0.84 (section 3.3)
γ	Coefficient derived in warm-cold tests (section 3.5) or a coefficient in the *Nu*-*Re* relationship (section 5.2)
ρ	Liquid H_2O density = 1000 kg m^{-3} (assumed independent of temperature)
σ	Stefan-Boltzmann constant = 5.67x10^{-8} W m^{-2} K^{-4}

Subscripts

c	Indoor cold setting
d	Downwelling
IB	Ice-bulb
s	Painted-steel sheeting
u	Upwelling
w	Indoor warm setting
x	Property of air film adjacent to the hotplate surface: p_x = standard-atmosphere pressure at the altitude of the measurement. The following three film properties are held constant in calculation of the Reynolds number (section 3.6) and in calculation of the sensible power output due to molecular conduction (section 3.6): 1) temperature (T_x = 303.15 K), 2) dynamic viscosity (μ_x = 1.862x10^{-5} kg m^{-1} s^{-1}; Rogers and Yau (1989; their Table 7.1)), and 3) thermal conductivity (K_x = 2.63x10^{-2} J m^{-1} s^{-1} K^{-1}; Rogers and Yau (1989; their Table 7.1)).

Operator

<*y*>	Time average of property *y*

References

Albrecht, B., M. Poellot, and S.K. Cox, Pyrgeometer measurements from aircraft, Review of Scientific Instruments, 45, 33-38, 1974

Borkhuu, B., Snowfall at a high-elevation site: Comparisons of six measurement techniques, M.S. Thesis, Department of Atmospheric Science, University of Wyoming, 2009

Boudala, F.S., R.Rasmussen, G.A.Isaac, and B.Scott, Performance of hot plate for measureing solid precipitation in complex terrain during the 2010 Vancouver Winter Olympics, J. Atmos.Oceanic Technol., 31, 437-446, 2014

Brandes, E.A., K. Ikeda, G. Zhang, M. Schonhuber, and R.M. Rasmussen, A statistical and physical description of hydrometeor distributions in Colorado snowstorms using a video disdrometer, J. Appl. Meteor. Climatol., 46, 634- 650, 2007

Campbell, L.S., W.J. Steenburgh, P.G. Veals, T.W. Letcher, and J.R. Minder, Lake-Effect Mode and Precipitation Enhancement over the Tug Hill Plateau during OWLeS IOP2b, Mon. Wea. Rev., 144, 1729–1748, doi: 10.1175/MWR-D-15-0412.1, 2016

Currie, I., Snow in the rain gauge (photograph), Weather, 53, 100, 1989

Deshler, T., Corrections of surface particle probe measurements for the effects of aspiration, J. Atmos.Oceanic Technol., 5, 547–560, 1988

Goodison, B.E., P. Y. T. Louie, and D. Yang, WMO solid precipitation measurement intercomparison. WMO Tech. Doc. 872, 211 pp., 1998

Hansen, L.G. and B.W. Webb, Air jet impingement heat transfer from modified surfaces, International Journal of Heat and Mass Transfer, 36, 989-997, 1992

Hass, G., Filmed surfaces for reflecting optics, Journal of the Optical Society of America, 45, 945-952, 1955

Havilcek, L.L., and R.D. Crain, *Practical Statistics for the Physical Sciences*, American Chemical Society, 1988

Iribarne, J.V., and W.L.Godson, *Atmospheric Thermodynamics*, 2nd ed., Reidel, 1981

Jevons,W. S., On the deficiency of rain in an elevated rain gauge as caused by wind, London Edinburgh Dublin Philos. Mag., 22, 421–433, 1861

King, W.D., D.A. Parkin, and R.J. Handsworth, A hot-wire liquid water device having fully calculable response characteristics, J. Appl. Meteor., 17, 809-813, 1978

Kobus, C.J. and G.L.Wedekind, An experimental investigation into forced, natural and combined forced and natural convective heat transfer from stationary isothermal circular disks, Int. J. Heat Mass Transfer, 38, 3329-3339, 1995

Lempio, G.E., K. Bumke, and A. Macke, Measurement of solid precipitation with an optical disdrometer, Advances in Geosciences, 10, 91-97, 2007

Locatelli, J.D. and P.V.Hobbs, Fall speeds and masses of solid precipitation particles, J. Geophys. Res., 79, 2185-2197, 1974

Loffler-Mang, M. and J. Joss, An optical disdrometer for measuring size and velocity of hydrometeors, J. Atmos.Oceanic Technol., 17, 130-139, 2000

Lovblad, G., J.W. Erisman, and D. Fowler, Deposition monitoring. Models and Methods for the Quantification of Atmospheric Input to Ecosystems, Chapter 3, The Nordic Council of Ministers, 37-41, 1993

Nespor, V., and B. Servuk, Estimation of wind-induced error of rainfall gauge measurements using a numerical simulation, J. Atmos.Oceanic Technol., 16, 450-464, 1999

Panofsky, H.A. and J.A.Dutton, *Atmospheric Turbulence*, Wiley-Interscience, New York, pp. 397, 1984

Rasmussen, R.M., J. Hallett, R. Purcell, S.D. Landolt, and J. Cole, The hotplate precipitation gauge, J. Atmos.Oceanic Technol., 28, 148-164, 2011

Rasmussen, R., B. Baker, J. Kochendorfer, T. Meyers, S. Landolt, A.P. Fischer, J. Black, J.M. Theriault, P. Kucera, D. Gochis, C. Smith, R. Nitu, M. Hall, K, Ikeda, and E. Gutmann, How well are we measuring snow?, Bull. Amer. Meteor. Soc., 93, 811-829, 2012

Rogers, R.R. and M.K. Yau, *A Short Course in Cloud Physics*, 3rd ed. Permagon Press, 304 pp., 1989

Steenburgh, J., L.Campbell, and P. Veals, North Redfield Snow Study Station, http://data.eol.ucar.edu/datafile/nph-get/382.023/Redfield_met_stn_readme.pdf, 2014

Stickel, J., B.Maloney, C.Pape and D.Burkheimer, Evaluation of the hotplate snow gauge, Center for Transportation Research and Education, Iowa State University, Aurora Project 2004-01, 2005

Thériault, J.M, R.Rasmussen, K.Ikeda, and S.Landolt, Dependence of snow gauge collection efficiency on snowflake characteristics, J. Appl. Meteor. Climatol., 745-762, 2012

Warnick, C.C., Rime ice and snow capping on high altitude precipitation gages, Proceedings of the 25th Annual Western Snow Conference, Santa Barbara, California, Western Snow Conference, 24-34, 1957

Weast, R.C., Ed.,Handbook of Chemistry and Physics, 56th ed, Chemical Rubber Company, 2350 pp., 1975

Wettlaufer, A., A fully compensated algorithm for the hotplate precipitation sensor, M.S. Thesis, Department of Atmospheric Science, University of Wyoming, 2013

Wolfe, J.P., and J.R.Snider, A Relationship between Reflectivity and Snow Rate for a High-Altitude S-Band Radar, J. Appl. Meteor. Climatol., 51, 1111–1128, 2012

World Meteorological Organization (WMO), Guide to Meteorological Instruments and Methods of Observation, Geneva, Switzerland, Chapter 6, Part I Measurement of Meteorological Variables, 2008

YES, INC., TPS-3100 Total Precipitation Sensor, Installation and User Guide, Version 2.0, Rev M, 43 pp., 2011

Young, H.D., *Statistical Treatment of Experimental Data*, McGraw-Hill Book Company, pp. 172, 1962

Atmos. Meas. Tech. Discuss., https://doi.org/10.5194/amt-2017-234
Manuscript under review for journal Atmos. Meas. Tech.
Discussion started: 30 August 2017

Atmospheric Measurement Techniques
Discussions
Open Access
EGU

Top and Bottom Plates
(Precipitation Sensor)

Longwave and Shortwave
Radiation Sensors

Temperature Sensor

Electronics

Figure 1 – The Yankee Environmental Systems TPS-3100 Total Precipitation Sensor with longwave and shortwave radiation sensors.

Figure 2 – Picture taken during indoor testing showing a hotplate's precipitation sensor positioned between top and bottom painted-steel sheets.

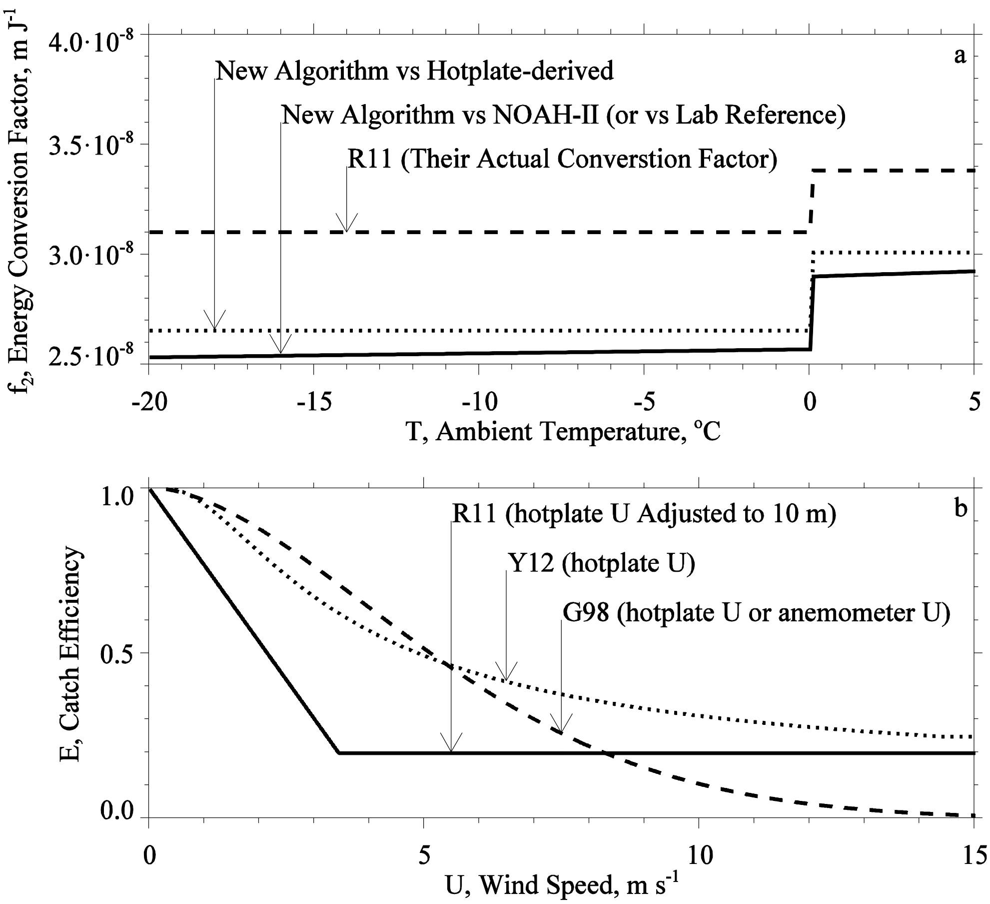

Figure 3 – a) Electrical-to-precipitation conversion factors vs ambient temperature assuming snow at $T < 0$ °C and rain at $T > 0$ °C. See text for details. b) Snow particle catch efficiency vs wind speed using the R11, Y12, and G98 formulations discussed in the text.

Atmos. Meas. Tech. Discuss., https://doi.org/10.5194/amt-2017-234
Manuscript under review for journal Atmos. Meas. Tech.
Discussion started: 30 August 2017

Atmospheric Measurement Techniques Discussions

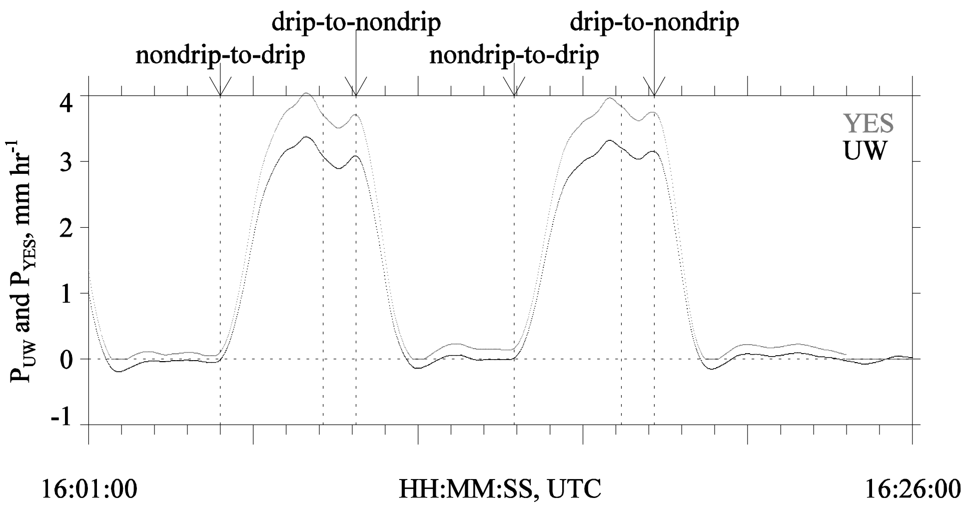

Figure 4 – Precipitation rates, derived using the UW and YES algorithms, plotted vs time. The figure shows two drip periods (starting at the nondrip-to-drip transitions), both with the reference set at 3.1 mm hr^{-1}, and nondrip periods (starting at the drip-to-nondrip transitions). Dashed vertical lines indicate the transitions and 1-min precipitation averaging intervals. Measurements are from the UW hotplate operating indoors on 20120229. The UW/GLE calibration constants (Table 3) and an f_2 derived with the second of two methods (section 3.7) were applied in the UW algorithm.

Atmos. Meas. Tech. Discuss., https://doi.org/10.5194/amt-2017-234
Manuscript under review for journal Atmos. Meas. Tech.
Discussion started: 30 August 2017

Atmospheric Measurement Techniques Discussions

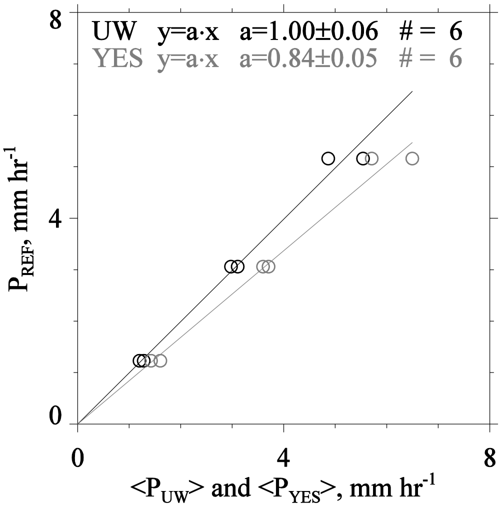

Figure 5 - Reference precipitation rate vs time-averaged P_{UW} and P_{YES}. Measurements are from the UW hotplate operating indoors on 20120229. The UW/GLE calibration constants (Table 3) and an f_2 derived with the second of two methods (section 3.7) were applied in the UW algorithm. Regression lines were forced through the origin and *x* deviations (horizontal departures of data from regression line) were used as the basis for the least squares criterion of best fit (Young, 1962). Standard deviations on the fitted ratios (confidence intervals) were derived using Student's t-distribution at the 95% level (Havilcek and Crain, 1988).

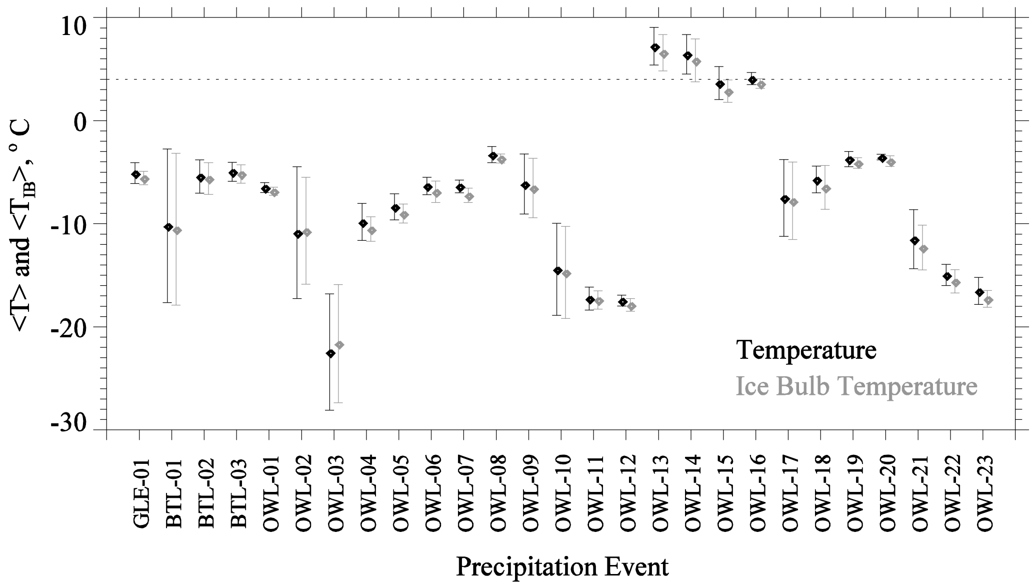

Figure 6 – Event-averaged ambient temperature (<*T*>) and event-averaged ambient ice bulb temperature (<T_{IB}>). The abscissa shows the 27 precipitation events in the order presented in Table 5. Error bars are ± 2 standard deviations. The dashed horizontal line is drawn at +4 °C.

Atmos. Meas. Tech. Discuss., https://doi.org/10.5194/amt-2017-234
Manuscript under review for journal Atmos. Meas. Tech.
Discussion started: 30 August 2017

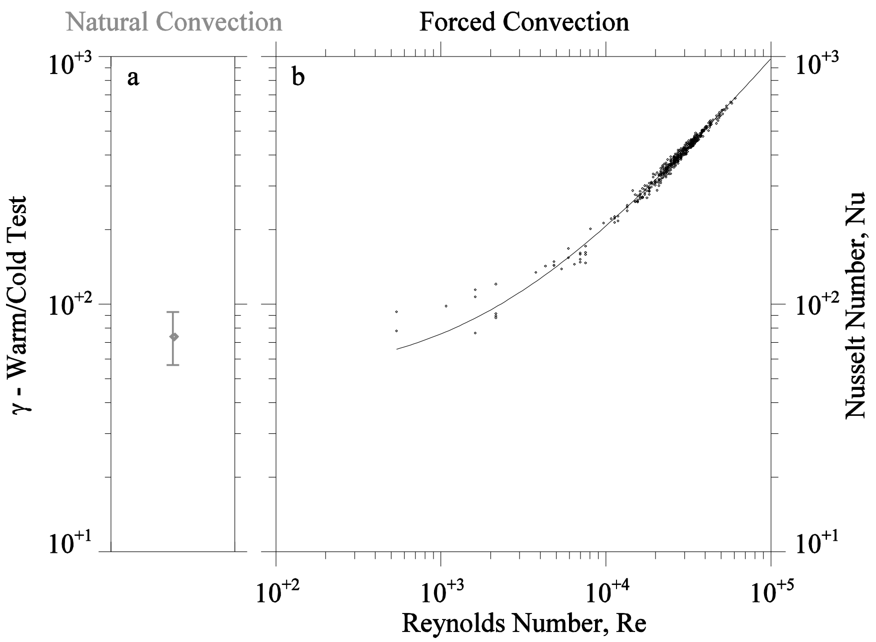

Figure 7 – a) γ from the warm-cold test summarized in the second row of Table 3. Error limits were derived by perturbing $Q_{top,w}$ (i.e., the value acquired in the warm test) by ± 0.5 W and repeating the analysis based on Eq. 7a - b. b) *Nu* vs *Re* scatterplot and fit curve for the UW hotplate at the GLE site. For clarity, only every fortieth *Nu*-*Re* data pair is plotted. The minimum *Re* plotted (data and fit function) corresponds to the minimum *U* reported in the UHP file (0.1 m s^{-1}). The measurement interval is 20120402 04:00 UTC to 20120402 09:00 UTC at the GLE site. The UW/GLE T_h (Table 3) was applied in the data analysis.

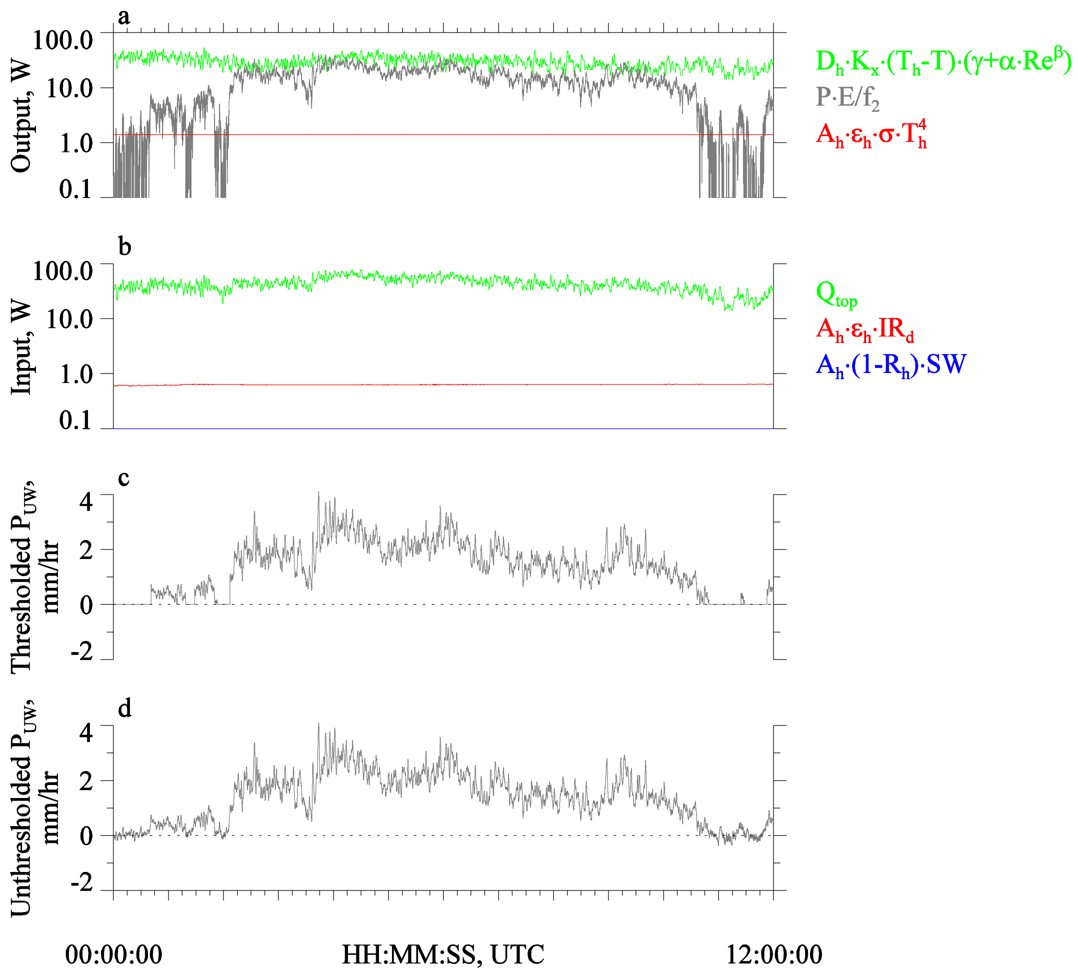

Figure 8 – Hotplate properties during rain (event = OWL-15 in Fig. 6 and Table 5). Because this event classifies as rain, *E* = 1 was applied in the UW algorithm. a) Power output terms in the Eq. 3; i.e., the sensible, latent, and upwelling longwave terms. b) Power input terms in the Eq. 3; i.e., the top plate power, downwelling longwave, and shortwave terms. The shortwave term is zero for this nighttime example, but is set to 0.1 W in the plot. c) Thresholded precipitation rate. d) Unthresholded precipitation rate.

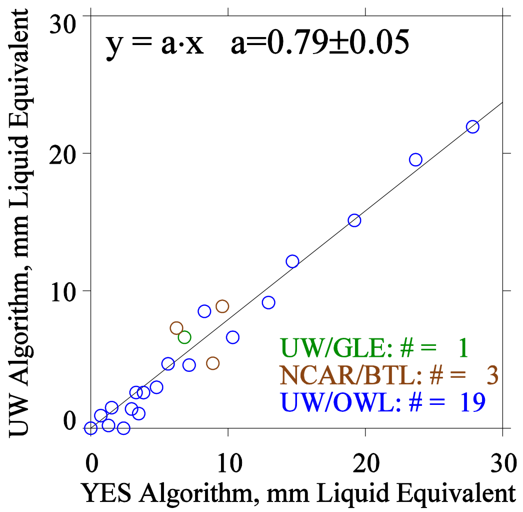

Figure 9 – Snow accumulations derived using the UW algorithm vs snow accumulations derived using the YES algorithm. Both the Y12 catch efficiency function and an f_2 derived with the first of two methods discussed in section 3.7 were applied in the UW algorithm. The regression line was forced through the origin and *y* deviations (vertical departures of data from regression line) were used as the basis for the least squares criterion of best fit (Young, 1962). The standard deviation on the fitted ratio (confidence interval) was derived using Student's t-distribution at the 95% level (Havilcek and Crain, 1988).

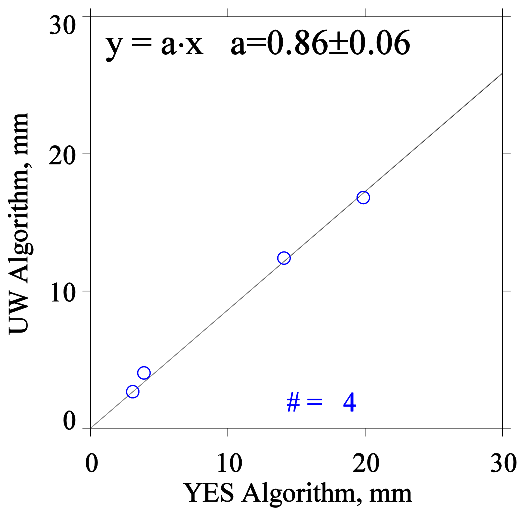

Figure 10 – Rain accumulations derived using the UW algorithm vs rain accumulations derived using the YES algorithm. An f_2 derived with the first of two methods discussed in section 3.7 was applied in the UW algorithm. Regression lines were forced through the origin and *y* deviations (vertical departures of data from regression line) were used as the basis for the least squares criterion of best fit (Young, 1962). The standard deviations on the fitted ratios (confidence intervals) were derived using Student's t-distribution at the 95% level (Havilcek and Crain, 1988).

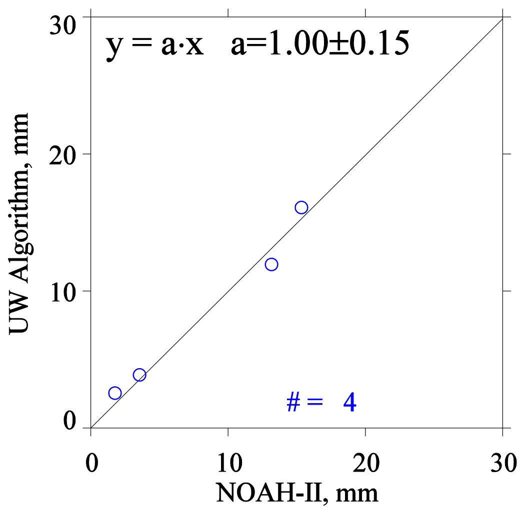

Figure 11 –Rain accumulations derived using the UW algorithm vs rain accumulations from the NOAH-II gauge. An f_2 derived with the second of two methods discussed in section 3.7 was applied in the UW algorithm. Regression lines were forced through the origin and *y* deviations (vertical departures of data from regression line) were used as the basis for the least squares criterion of best fit (Young, 1962). The standard deviations on the fitted ratios (confidence intervals) were derived using Student's t-distribution at the 95% level (Havilcek and Crain, 1988).

Atmos. Meas. Tech. Discuss., https://doi.org/10.5194/amt-2017-234
Manuscript under review for journal Atmos. Meas. Tech.
Discussion started: 30 August 2017

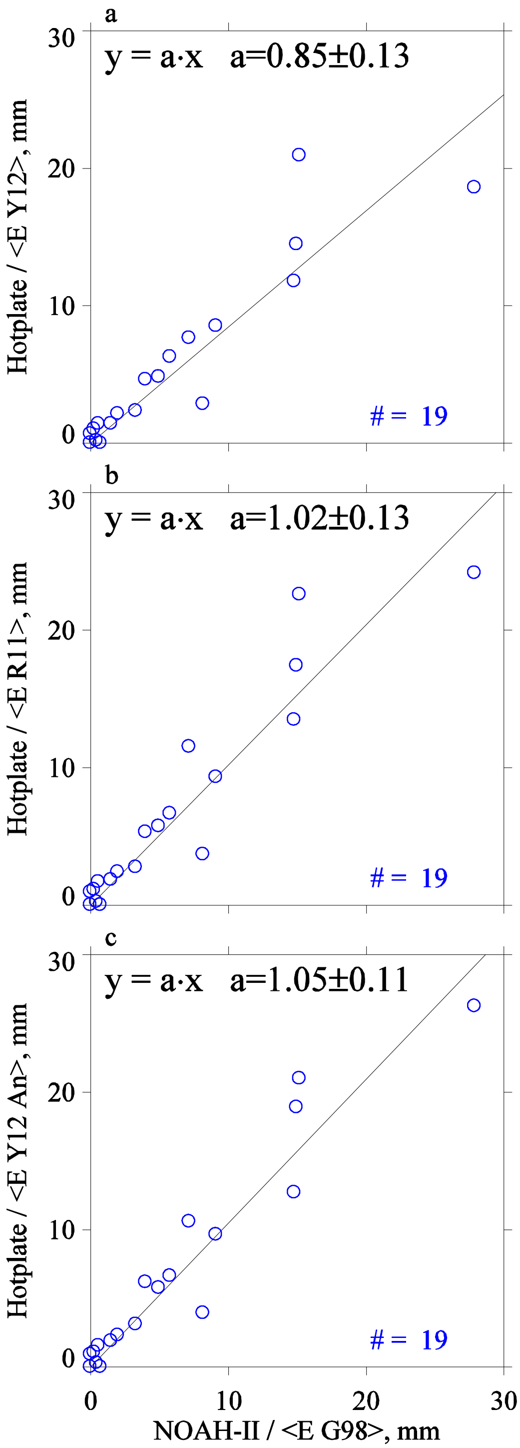

Figure 12 – UW hotplate and NOAH-II measurements of snow (liquid-equivalent accumulations, not corrected for inefficient catch, divided by an event-averaged snow particle catch efficiency) at OWL. An f_2 derived with the second of two methods discussed in section 3.7 was applied in the UW algorithm. Regression lines were forced through the origin and *y* deviations (vertical departures of data from regression line) were used as the basis for the least squares criterion of best fit (Young, 1962). The standard deviations on the fitted ratios (confidence intervals) were derived using Student's t-distribution at the 95% level (Havilcek and Crain, 1988).

Table 1 – Hotplate Data Files

Recorded Variable [a], dimension	File UHP	File SHP	Symbol
Unix Time, s	✓	✓	
Precip. Rate, mm hr^{-1}	✓		P_{YES}
Accumulated Precip., mm	✓		
Ambient Temp., °C	✓	✓	T
Enclosure Temp., °C	✓	✓	
Wind Speed, m s^{-1}	✓		U
Shortwave Radiation, W m^{-2}	✓	✓	SW
Net Longwave Radiation, W m^{-2}	✓	✓	M_{IR}
Barometric Pressure, hPa	✓	✓	p [b]
RH Sensor Temp., °C	✓	✓	
RH, %	✓	✓	RH
Top Plate Voltage, V		✓	
Bottom Plate Voltage, V		✓	
Top Plate Current, A		✓	
Bottom Plate Current, A		✓	
Top Plate Resistance, Ω		✓	
Bottom Plate Resistance, Ω		✓	
Top Plate Power, W		✓	Q_{top}
Bottom Plate Power, W		✓	Q_{bot}
Radiation Sensors' Temp., °C		✓	

[a] With the exception of Unix time, all recorded variables are 60-s running averages, sampled at 1 Hz (YES, 2011)

[b] Although pressure is a recorded variable, the pressure used in the UW algorithm (p_x; section 3.6 and Appendix) is the standard-atmosphere pressure at the altitude of the measurement

Table 2 – Field Sites, Site Location, Vegetation at the Site, Gauge Location, Number of Events, and Event Type

Site Abbreviation Site Reference Hotplate	Site Location	Height of Vegetation, m AGL	Gauge Location at Site	Precipitation Events
GLE Wettlaufer (2013) UW	SE Wyoming 106.240 °W 41.3665 °N 3190 m MSL	10 to 20 m	Hotplate: 27 m AGL on top deck of a meteorological tower [a] NOAH-II: 3 m AGL (clearing in conifer forest 80 m SE of tower)	1 Snow
BTL Wettlaufer (2013) NCAR	SE Wyoming 106.975 °W 41.1558 °N 3010 m MSL	10 to 20 m	Clearing in conifer forest Hotplate: 3 m AGL NOAH-II: 3 m AGL	3 Snow
OWL Steenburgh et al. (2014) UW	NW New York 75.8771 °W 43.6245 °N 385 m MSL	2 to 5 m	Clearing in deciduous brush and deciduous trees Hotplate: 1.7 m AGL [b] and 2.5 m AGL [c] NOAH-II: 2.5 m AGL	4 Rain 19 Snow

[a] This is the Brooklyn Lake, Wyoming AmeriFlux Tower; AmeriFlux is a network of sites that measure energy and trace-gas fluxes.

[b] First 7 of 23 OWL precipitation events (Date < 20131217)

[c] Last 16 of 23 OWL precipitation events (Date > 20131217)

Table 3 – Summary of Warm-cold Tests

Indoor Calibration (Warm-cold Tests)			
Year	Hotplate/Field Site	T_{hp}, °C	γ
2012	NCAR/BTL	42.2 ± 7.4 [a]	106. ± 15.1 [a]
2012 - 2013	UW/GLE	52.2 ± 15.7	74.8 ± 18.1
2013 - 2015	UW/OWL	66.5 ± 7.8	57.8 ± 7.7

[a] Error limits derived by perturbing $Q_{top,w}$ (i.e., the value acquired in the warm test) by ± 0.5 W and repeating the analysis based on Eq. 7a - b.

Atmos. Meas. Tech. Discuss., https://doi.org/10.5194/amt-2017-234
Manuscript under review for journal Atmos. Meas. Tech.
Discussion started: 30 August 2017

Atmospheric Measurement Techniques Discussions

Table 4 – Summary of Drip Tests

Indoor Calibration (Drip Tests)				
Year	Hotplate/Field Site	P_{REF} vs $<P_{UW}>$ ratio [a]	P_{REF} vs $<P_{YES}>$ ratio [a]	# [b]
2012	NCAR/BTL	0.99 ± 0.02	0.81 ± 0.03	6
2012 - 2013	UW/GLE	1.00 ± 0.06	0.84 ± 0.05	6
2013 - 2015	UW/OWL	0.97 ± 0.04	0.79 ± 0.03	6

[a] Ratios were derived as the slope of a regression lines forced through the origin. The *x* deviations (horizontal departures of data from regression line) were used as the basis for the least squares criterion of best fit (Young, 1962). Standard deviations on the fitted ratios (confidence intervals) were derived using Student's t-distribution at the 95% level (Havilcek and Crain, 1988).

[b] # = number of tests.

Table 5 – Precipitation Events

Precipitation Event	Start Date, YYYYMMDD UTC	Start Time, HH:MM UTC	End Time HH:MM UTC	<T> [a], °C	<T_{IB}> [b], °C	<U> [c], m s^{-1}	UW [d], mm	YES [d], mm	<E Y12> [e]	<E Y12 An> [f]	<E R11> [g]	NOAH-II [d], mm	<E G98> [h]
GLE-01	20120414	0:00	13:00	-5.1	-5.6	1.8	5.6	6.0	0.84	NA [i]	NAP [j]	7.3	0.89
BTL-01	20120116	11:00	1:00	-10.2	-10.5	2.0	3.8	7.5	0.80	NA	NAP	8.0	0.87
BTL-02	20120119	8:00	18:00	-5.4	-5.6	4.3	3.8	3.4	0.55	NA	NAP	1.0	0.60
BTL-03	20120120	7:00	18:00	-5.0	-5.2	2.4	6.3	7.1	0.75	NA	NAP	8.2	0.83
OWL-01	20131211	18:00	0:00	-6.5	-6.9	1.4	16.9	21.5	0.91	0.64	0.70	20.0	0.72
OWL-02	20131212	0:00	6:00	-10.9	-10.7	0.4	1.0	3.5	0.99	0.94	0.90	0.3	0.96
OWL-03	20131212	6:00	12:00	-22.5	-21.6	0.3	0.0	2.4	1.00	1.00	0.93	0.0	1.00
OWL-04	20131212	18:00	0:00	-9.8	-10.5	1.3	0.2	1.2	0.90	0.53	0.67	0.3	0.57
OWL-05	20131213	6:00	12:00	-8.4	-9.0	0.9	13.9	18.5	0.96	0.73	0.80	12.1	0.81
OWL-06	20131215	19:45	0:00	-6.3	-6.9	0.9	1.3	2.9	0.94	0.85	0.78	0.5	0.88
OWL-07	20131216	0:00	6:00	-6.4	-7.3	0.3	20.9	27.8	1.00	1.00	0.93	15.2	1.00
OWL-08	20131218	18:00	0:00	-3.3	-3.7	1.5	10.4	13.2	0.88	0.82	0.77	12.9	0.87
OWL-09	20140106	18:00	0:00	-6.2	-6.5	3.9	4.5	4.6	0.58	0.42	0.39	2.5	0.35
OWL-10	20140107	0:00	6:00	-14.4	-14.7	3.8	0.4	0.3	0.60	0.44	0.42	0.0	0.38
OWL-11	20140107	6:00	12:00	-17.3	-17.4	3.0	1.9	3.3	0.67	0.49	0.52	4.0	0.49
OWL-12	20140107	18:00	0:00	-17.5	-17.9	3.9	0.0	0.0	0.58	0.42	0.39	0.3	0.35
OWL-13	20140111	15:45	21:00	7.2	6.6	1.1	11.9	14.1	1.00	1.00	1.00	13.2	1.00
OWL-14	20140111	23:00	2:00	6.4	5.8	2.4	3.9	3.9	1.00	1.00	1.00	3.5	1.00
OWL-15	20140114	0:00	12:00	3.7	2.9	0.9	16.1	19.9	1.00	1.00	1.00	15.3	1.00
OWL-16	20140114	12:45	15:45	4.1	3.6	1.2	2.6	3.1	1.00	1.00	1.00	1.8	1.00
OWL-17	20140119	0:00	12:00	-7.5	-7.8	1.3	1.9	3.3	0.91	0.84	0.81	1.8	0.88
OWL-18	20140119	18:00	0:00	-5.7	-6.5	1.9	1.9	2.6	0.81	0.61	0.69	2.3	0.69
OWL-19	20140120	0:00	2:00	-3.7	-4.1	3.1	0.9	1.0	0.67	0.50	0.52	0.8	0.51
OWL-20	20140120	2:00	12:00	-3.5	-3.9	2.1	3.8	4.8	0.78	0.66	0.66	3.5	0.72
OWL-21	20140127	18:00	0:00	-11.5	-12.3	1.7	4.0	6.6	0.86	0.65	0.75	2.8	0.69
OWL-22	20140128	0:00	6:00	-15.0	-15.6	0.4	6.3	10.3	1.00	0.95	0.94	5.6	0.96
OWL-23	20140128	6:00	12:00	-16.5	-17.3	0.9	8.0	12.1	0.94	0.83	0.86	8.1	0.88

[a] Event-averaged ambient temperature
[b] Event-averaged ice bulb temperature
[c] Event-averaged hotplate *U*
[d] Liquid-equivalent precipitation amount not corrected for inefficient catch (UW values are computed with an f_2 derived with the second of two methods discussed in section 3.7)
[e] Event-averaged snow particle catch efficiency derived using Y12 and the hotplate *U*
[f] Event-averaged snow particle catch efficiency derived using Y12 and the anemometer *U*
[g] Event-averaged snow particle catch efficiency derived using R11 and hotplate *U* adjusted to 10 m AGL
[h] Event-averaged snow particle catch efficiency derived using G98 and hotplate *U* (GLE and BTL) or anemometer *U* (GLE)
[i] NA = not available
[j] NAP = not applicable

Table 6 – Summary of Fitted *Nu-Re* Coefficients

Field Calibration (*Nu* - *Re* Coefficients)			
Hotplate/Field Site	γ	α	β
NCAR/BTL [a]	86.2	0.126	0.781
UW/GLE [b]	49.1	0.130	0.771
UW/OWL [c]	45.6	0.172	0.713

[a] NCAR hotplate; measurement interval 20120118 23:00 UTC to 20120119 5:00 UTC

[b] UW hotplate; measurement interval 20120402 04:00 UTC to 20120402 09:00 UTC

[c] UW hotplate; measurement interval 20140107 18:00 UTC to 20140108 08:00 UTC